Check for updates

Mask-aligner lithography using a continuous-wave diode laser frequency-quadrupled to 193 nm

RAOUL KIRNER,[1,6,7] ANDREAS VETTER,[1,2,6] DMITRIJS OPALEVS,[3] CHRISTIAN GILFERT,[3] MATTHIAS SCHOLZ,[3] PATRICK LEISCHING,[3] TORALF SCHARF,[4] WILFRIED NOELL,[1] CARSTEN ROCKSTUHL,[2,5] AND REINHARD VOELKEL[1]

[1]SUSS MicroOptics SA, Rouges-Terres 61, CH-2068 Hauterive, Switzerland
[2]Institute of Nanotechnology (INT), Karlsruhe Institute of Technology, Hermann-von-Helmholtz-Platz 1, 76344 Eggenstein-Leopoldshafen, Germany
[3]TOPTICA Photonics AG, Lochhamer Schlag 19, 82166 Gräfelfing, Germany
[4]Nanophotonics and Metrology Laboratory, École Polytechnique Fédérale de Lausanne (EPFL), CH-1015 Lausanne, Switzerland
[5]Institute of Theoretical Solid State Physics (TFP), Karlsruhe Institute of Technology, Wolfgang-Gaede-Strasse 1, 76131 Karlsruhe, Germany
[6]Both authors contributed equally
[7]raoul.kirner@suss.com

Abstract: We present a mask-aligner lithographic system operated with a frequency-quadrupled continuous-wave diode laser emitting at 193 nm. For this purpose, a 772 nm diode laser is amplified by a tapered amplifier in the master-oscillator power-amplifier configuration. The emission wavelength is upconverted twice, using LBO and KBBF nonlinear crystals in second-harmonic generation enhancement cavities. An optical output power of 10 mW is achieved. As uniform exposure field illumination is crucial in mask-aligner lithography, beam shaping is realized with optical elements made from fused silica and CaF_2 featuring a diffractive non-imaging homogenizer. A tandem setup of shaped random diffusers, one static and one rotating, is used to control speckle formation. We demonstrate first experimental soft contact and proximity prints for a field size of $1 \, cm^2$ with a standard binary photomask and proximity prints with a two-level phase mask, both printed into 120 nm layers of photoresist on unstructured silicon substrates.

References and links

1. L. Stürzebecher, F. Fuchs, U. D. Zeitner, and A. Tünnermann, "High-resolution proximity lithography for nano-optical components," Microelectron. Eng. **132**, 120–134 (2015).
2. R. Völkel, U. Vogler, A. Bich, P. Pernet, K. J. Weible, M. Hornung, R. Zoberbier, E. Cullmann, L. Stürzebecher, T. Harzendorf, and U. D. Zeitner, "Advanced mask aligner lithography: new illumination system," Opt. Express **18**, 20968–20978 (2010).
3. K. Jain, C. Willson, and B. Lin, "Ultrafast deep UV Lithography with excimer lasers," IEEE Electron Device Lett. **3**, 53–55 (1982).
4. K. Jain, "Advances In Excimer Laser Lithography," Proc. SPIE **774**, 115 (1987).
5. T. Saito, T. Matsunaga, K.-i. Mitsuhashi, K. Terashima, T. Ohta, A. Tada, T. Ishihara, M. Yoshino, H. Tsushima, T. Enami, H. Tomaru, and T. Igarashi, "Ultranarrow-bandwidth 4-kHz ArF excimer laser for 193-nm lithography," Proc. SPIE **4346**, 1229 (2001).
6. V. B. Fleurov, D. J. Colon III, D. J. W. Brown, P. O'Keeffe, H. Besaucele, A. I. Ershov, F. Trintchouk, T. Ishihara, P. Zambon, R. J. Rafac, and A. Lukashev, "Dual-chamber ultra line-narrowed excimer light source for 193-nm lithography," Proc. SPIE **5040**, 1694 (2003).
7. S. Partel, S. Zoppel, P. Hudek, A. Bich, U. Vogler, M. Hornung, and R. Völkel, "Contact and proximity lithography using 193nm Excimer laser in Mask Aligner," Microelectron. Eng. **87**, 936–939 (2010).

8. D. Basting and G. Marowsky, eds., *Excimer Laser Technology* (Springer, 2005).

9. M. Mizuguchi, H. Hosono, H. Kawazoe, and T. Ogawa, "Color center formation and time-resolved photoluminescence for ArF excimer laser irradiation in CaF2 single crystals," Proc. SPIE **3424**, 60 (1998).

10. R. E. Schenker, L. Eichner, H. Vaidya, S. Vaidya, and W. G. Oldham, "Degradation of fused silica at 193 nm and 213 nm," Proc. SPIE **2440**, 118 (1995).

11. J. M. Algots, R. Sandstrom, W. N. Partlo, P. Maroevic, E. Eva, M. Gerhard, R. Linder, and F. Stietz, "Compaction and rarefaction of fused silica with 193-nm excimer laser exposure," Proc. SPIE **5040**, 1639 (2003).

12. D. Opalevs, M. Scholz, C. Gilfert, R. Li, X. Wang, L. Liu, A. Vetter, R. Kirner, T. Scharf, W. Noell, C. Rockstuhl, R. Völkel, and P. Leisching, "Semiconductor-based narrow-line and high-brilliance 193nm laser system for industrial applications," submitted.

13. M. Scholz, D. Opalevs, P. Leisching, W. Kaenders, G. Wang, X. Wang, R. Li, and C. Chen, "A bright continuous-wave laser source at 193 nm," Appl. Phys. Lett. **103**, 051114 (2013).

14. C. Mack, *Fundamental Principles of Optical Lithography* (John Wiley & Sons, 2007).

15. C. Chen, Y. Wang, Y. Xia, B. Wu, D. Tang, K. Wu, Z. Wenrong, L. Yu, and L. Mei, "New development of nonlinear optical crystals for the ultraviolet region with molecular engineering approach," J. Appl. Phys. **77**, 2268 (1995).

16. D. Tang, Y. Xia, B. Wu, and C. Chen, "Growth of a new UV nonlinear optical crystal: $KBe_2(BO_3)F_2$," J. Cryst. Growth **222**, 125–129 (2001).

17. T. Kanai, X. Wang, S. Adachi, S. Watanabe, and C. Chen, "Watt-level tunable deep ultraviolet light source by a KBBF prism-coupled device." Opt. Express **17**, 8696–8703 (2009).

18. S. Tanaka, M. Arakawa, A. Fuchimukai, Y. Sasaki, T. Onose, Y. Kamba, H. Igarashi, C. Qu, M. Tamiya, H. Oizumi, S. Ito, K. Kakizaki, H. Xuan, Z. Zhao, Y. Kobayashi, and H. Mizoguchi, "Development of high coherence high power 193nm laser," Proc. SPIE **9726**, 972624 (2016).

19. T. Weichelt, Y. Bourgin, and U. D. Zeitner, "Mask aligner lithography using laser illumination for versatile pattern generation," Opt. Express **25**, 20983–20992 (2017).

20. R. Völkel and K. J. Weible, "Laser beam homogenizing: limitations and constraints," Proc. SPIE **7102**, 71020J (2008).

21. R. Völkel, U. Vogler, A. Bich, K. J. Weible, M. Eisner, M. Hornung, P. Kaiser, R. Zoberbier, and E. Cullmann, "Illumination system for a microlithographic contact and proximity exposure apparatus," European Patent 2 253 997 A2 (2009).

22. P. Rai-Choudhury, ed., *Handbook of microlithography, micromachining, and microfabrication*, vol. 1 of *IEE materials & devices series ; SPIE Press monograph* (SPIE Optical Engineering Pr., 1997).

23. R. W. P. Drever, J. L. Hall, F. V. Kowalski, J. Hough, G. M. Ford, A. J. Munley, and H. Ward, "Laser phase and frequency stabilization using an optical resonator," Appl. Phys. B **31**, 97–105 (1983).

24. J. W. Goodman, *Speckle Phenomena in Optics : Theory and Applications* (Roberts & Co, 2007).

25. F. M. Dickey and T. E. Lizotte, *Laser Beam Shaping Applications* (CRC Press, 2017).

26. Q. B. Li and F. P. Chiang, "A New Formula for Fringe Localization in Holographic Interferometry," Opt. Lasers Eng. **9**, 137–157 (1988).

27. H. T. Yura, S. G. Hanson, R. S. Hansen, and B. Rose, "Three-dimensional speckle dynamics in paraxial optical systems," J. Opt. Soc. Am. A **16**, 1402–1412 (1999).

28. D. Li, D. P. Kelly, R. Kirner, and J. T. Sheridan, "Speckle orientation in paraxial optical systems," Appl. Opt. **51**, A1–A10 (2012).

29. F. M. Dickey, ed., *Laser Beam Shaping: Theory and Techniques* (CRC Press, 2017).

30. G. J. Swanson, "Binary optics technology: Theoretical limits on the diffraction efficiency of multilevel diffractive optical elements," Tech. rep., M.I.T. Lincoln Laboratory (1991).

31. N. G. Douglas, A. R. Jones, and F. J. van Hoesel, "Ray-based simulation of an optical interferometer," J. Opt. Soc. Am. A **12**, 124–131 (1995).

32. N. Lindlein and H. P. Herzig, "Design and modeling of a miniature system containing micro-optics," Proc. SPIE **4437**, 1 (2001).

33. N. Lindlein, "Simulation of micro-optical systems including microlens arrays," J. Opt. A: Pure Appl. Opt. **4**, S1–S9 (2002).

34. T. Ito and S. Okazaki, "Pushing the limits of lithography," Nature **406**, 1027–1031 (2000).

35. F. M. Schellenberg, "Resolution enhancement technology: the past, the present, and extensions for the future," Proc. SPIE **5377**, 1 (2004).

36. R. Völkel, U. Vogler, A. Bramati, T. Weichelt, L. Stürzebecher, U. D. Zeitner, K. Motzek, A. Erdmann, M. Hornung, and R. Zoberbier, "Advanced mask aligner lithography (AMALITH)," Proc. SPIE **20**, 83261Y (2012).

37. M. Lampton, "The Microchannel Image Intensifier," Scientific American **245**, 62–71 (1981).

38. T. Sannomiya, O. Scholder, K. Jefimovs, C. Hafner, and A. B. Dahlin, "Investigation of Plasmon Resonances in Metal Films with Nanohole Arrays for Biosensing Applications," Small **7**, 1653–1663 (2011).

1.   Introduction

Mask-aligner lithography is a microfabrication technique used in research and production to transfer a mask pattern to a photoresist-coated substrate [1]. Mask and wafer are arranged in close proximity or in contact to achieve full-field structuring with a modest resolution at low costs and high flexibility. While contact lithography offers higher resolution, possible damage to mask and photoresist layer, decreasing both yield and mask lifetime, inhibit its use for most production scenarios. For both contact and proximity mask-aligner lithography, the resolution scales with wavelength. Modern mask-aligners mainly rely on high-pressure mercury arc lamp illumination sources (g-, h-, i-line; 436, 405, and 365 nm), since these offer high intensities at low cost and complexity [2].

The spatial resolution of the printing process in mask-aligner lithography can be improved by introducing a light source with a reduced wavelength. Using KrF and ArF excimer lasers, emitting in the mid- and deep-ultraviolet (MUV and DUV) at 248 nm and 193 nm and operated in a pulsed regime [3–6], in principle can be applied to mask-aligner lithography [7]. However, the actual integration is complex and expensive. Rather extreme conditions, such as corrosive and large volume gas mixtures at high pressures and voltages exceeding 40 kV, are required for high-power operation [8]. Moreover, in the DUV, feasible optical materials are restricted to crystalline calcium fluoride (CaF_2) and UV-grade fused silica. The formation of color centers emerging from the high peak powers in pulsed operation leads to a degradation in transmittance over time in such materials [9]. In SiO_2, a compaction of the optical material, arising from the high-energy pulses, results in a change of the refractive index and hence the imaging properties of the system [10, 11]. Quite a frequent maintenance, including gas exchange and electrode replacement, is furthermore required and adds to complexity and cost when using such KrF and ArF excimer lasers.

To entirely mitigate these problems we present here a novel approach for a mask-aligner illumination that relies on a frequency-quadrupled continuous-wave (CW) diode laser as light source [12]. The source has a monomodal stable output at 193 nm [13]. This wavelength is chosen for its compatibility to the photolithography technology developed for the ArF excimer laser, especially the photoresist chemistry tailored to work in the specified illumination regime [14], with chemically amplified resists necessary for DUV wavelengths.

The generation of CW light relying on diode and solid-state lasers for wavelengths below 200 nm has been practically inhibited by the unavailability of suitable materials, i.e., nonlinear crystals with suitable frequency-conversion properties in the desired wavelength range. The introduction of high-quality potassium fluoro-beryllo-borate (KBBF) crystals has just been closing this gap [15–17].

Our light source features two second-harmonic generation (SHG) processes. In a first stage, the amplified emission of the 772 nm diode laser (*DL pro*, TOPTICA PHOTONICS) is converted to 386 nm in a lithium triborate (LBO) crystal. For the subsequent second SHG stage (386 nm to 193 nm conversion), a KBBF crystal is employed. The obtained maximum CW optical output power is 10 mW at the moment, but could be augmented to output powers exceeding 50 to 100 mW.

Up to now, the output of such a laser system is mainly used as seed laser for hybrid high-coherence pulsed excimer systems, as for example demonstrated in [18]. While featuring a narrow linewidth and high coherence at high output powers, the excimer amplifier is again complex and expensive. Our approach for mask-aligner lithography features a significant simplification, and the greatly reduced device dimensions allow a tabletop light source.

Two recent publications demonstrate mask-aligner lithography relying on laser illumination. Partel *et al.* introduced an excimer laser emitting at a wavelength of 193 nm to a mask-aligner [7]. Beam homogenization is realized using microlens arrays, while the broadband multimode spectrum of the source mitigates interference effects. Full-field patterning with critical dimensions

of 2 μm in 10 μm gap proximity lithography is demonstrated. Weichelt *et al.* use a laser source emitting at a wavelength of 355 nm, close to i-line illumination [19]. To avoid speckle formation, they implement a rotating holographic diffuser. In addition, a galvanometer scanner is used to shape the angular spectrum. While they report on pinhole Talbot lithography and complex lateral patterns, minimal critical dimensions and the uniformity of the full field are not discussed.

In our system, monomodal light generation results in a high brilliance, and consequently enables low-loss beam-shaping and -homogenization. The continuous emission offers a uniform power distribution in time, preventing short-termed heat peaks in optical elements, photomask, and photoresist. As for excimer lasers, the output has to be shaped and homogenized in order to obtain a two-dimensional flat-top illumination profile, i.e., uniform intensity and angular distribution in the photomask plane.

We present simulations and experimental results for the beam homogenization using a two-stage homogenizer setup with a diffractive optical element (DOE) and discuss its optical performance. The high coherence of the laser is undesired in mask-aligner lithography, since it results in the formation of speckle patterns in the wafer plane [20]. The application of shaped random diffusers to mitigate this problem is described. While our findings are obtained for a small print field of approximately 1 cm^2, the homogenization strategy can be extended to larger field sizes. A modification of the angular spectrum of the illumination is possible by means of mechanical apertures in the output plane of the first homogenizer [2, 21].

Proximity prints of resolution structures (lines and spaces, vias) using a standard amplitude mask are performed in a mask-aligner. The mask-aligner is outfitted with a reflectometric measurement system for exposure gap control [1] and, together with a high-precision six-axis stage, offers sub-micron positioning capabilities. In addition, parallel lines and spaces as well as hexagonal dot arrays using a chromeless binary phase mask are demonstrated.

All together, we document in this contribution how an entire mask-aligner photolithographic system operating with a continuous high-power light source emitting at a wavelength of 193 nm has to look like. The successful demonstration of actual lithographically fabricated samples paves the way for such technology towards future exploration. To document such a system, we start by explaining the details of the source in section 2, outline the details of the beam shaping and the control of its coherence properties in section 3, and detail the lithographic results in a finalizing section.

2. DUV mask-aligner photolithography with continuous-wave laser illumination

2.1. Mask-aligner lithography

As mentioned before, mask-aligner photolithography allows for the full-field transfer of structural information of a photomask to a photosensitive target, e.g. a photoresist-coated substrate. Contact exposure, while offering the best resolution in the range of the illumination wavelength, is frequently not the best choice in most production environments as resist sticking to the mask reduces reproducibility, yield, and, in consequence mask lifetime.

All these problems are avoided when using proximity printing which usually implies gaps between mask and wafer in the range of 20 μm to 50 μm. Here, resolution is limited by diffraction at the mask structures. The achievable resolution follows the relation

$$\text{Resolution} \sim \sqrt{g \cdot \lambda} \tag{1}$$

with the proximity gap g and the exposure wavelength λ [22].

As readily seen from relation (1), there are two possibilities to increase the resolution of proximity printing: to decrease the gap and/or the exposure wavelength. As the gap is limited by substrate flatness and similar factors to a minimum of approximately 20 μm, the natural choice is to deploy illumination sources with shorter wavelengths than those of typical light sources for mask-aligners such as mercury high-pressure arc lamps.

Typically, lithographic exposure requires a uniform intensity distribution in the mask plane, a top-hat beam profile in the ideal case. In addition, telecentric illumination with uniform angular spectrum is generally desired. We investigate a concept of laser beam shaping applied to a highly coherent source to enforce these desired properties.

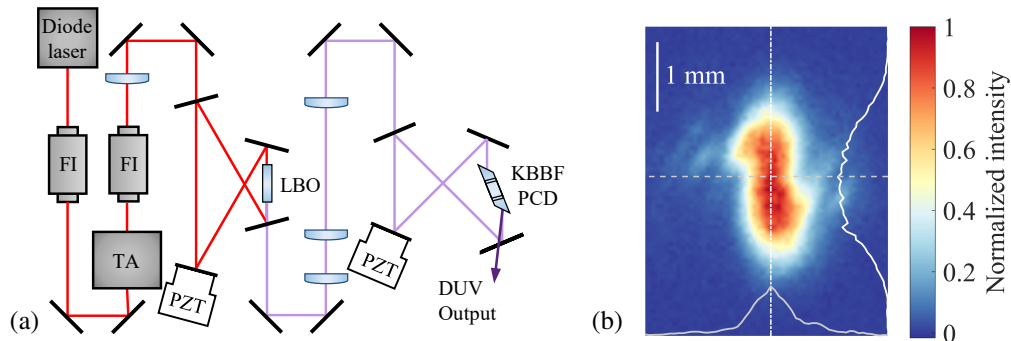## 2.2. Mask-aligner illumination in the deep-ultraviolet regime

Fig. 1. (a) Schematic layout of the 193 nm CW laser. The output of a diode laser is routed through a Faraday isolator (FI) and magnified in a tapered amplifier (TA). For frequency conversion, a lithium triborate (LBO) and a potassium fluoro-beryllo-borate (KBBF) crystal is used. Active feedback control is implemented via piezo elements (PZT). Adapted from [13]. (b) Beam profile measured at the laser output.

To improve the printable resolution, we introduce here a semiconductor CW laser source with an emission wavelength of 193 nm [13] to a mask-aligner. Figure 1(a) depicts a schematic layout of the laser. The laser is realized according to the master-oscillator power-amplifier (MOPA) principle: a stabilized extended cavity diode laser with a narrow linewidth of less than 10 kHz at 772 nm acts as the seed laser, feeding a tapered amplifier which enhances the optical power to 3 W. Lenses are used to shape the beam profile prior the SHG cavities, and Faraday isolators are inserted to prevent back reflections into both the seed laser and the tapered amplifier. The first SHG stage consists of a bow-tie enhancement cavity with a LBO nonlinear crystal, which converts the input light to a wavelength of 386 nm. The second SHG stage uses a KBBF crystal sandwiched between two CaF_2 prisms to optically access the necessary crystal direction, also in a bow-tie cavity configuration. This stage results in an upconversion to the DUV emission wavelength of 193 nm. Both SHG cavities are stabilized via the Pound-Drever-Hall scheme using piezoelectric actuators [23]. The optical output power at the final wavelength depends most sensitively on the beam position in the KBBF crystal, and is typically 7 mW in a single fundamental mode, with a maximum of 10 mW for the crystal in use. While the power of the laser is orders of magnitude lower than achieved in current excimer technology, an upscaling is possible by improvements in the bonding of the KBBF crystal.

After the frequency quadrupling, the output beam still possesses a spectral linewidth of < 500 kHz [13], which is by far superior compared to standard high-pressure mercury arc lamps and even superior compared to a linewidth of 2.5 GHz for top-notch lithography [5].

The beam has an elliptic profile, imposed by the second SHG stage (DUV output direction not parallel to the pump laser direction, see [13]). Figure 1(b) depicts the beam profile 200 mm behind the laser output. To avoid contamination, the output facet is purged with nitrogen.

2.3. Coherence control

The monomodal laser light source features very high spatial and temporal coherence, which might result in unwanted interference effects. These manifest as speckle and coherent multiple reflections off the optical elements in the setup. Speckle cause a random amplitude and phase distribution forming the illumination pattern in the photomask plane and, consequently, in the photoresist. Interference fringes caused by multiple reflections also contribute to non-uniformities in the exposure of the photoresist.

To address both issues, the spatial coherence of the source needs to be reduced. For this reason, optical diffusers are placed directly after the beam outlet and alignment mirrors, as depicted schematically in Fig. 2(a). Here we use a tandem setup of randomly shaped diffusers manufactured by Suss MicroOptics SA, as shown in detail in Fig. 2(b). A white light interferometric image of the static diffuser reveals the surface height profile, as depicted in Fig. 3(a). From goniometric measurements, measured at 633 nm, we obtain a divergence angle of 0.59° for the first, static diffuser, while the second, rotating diffuser has a divergence angle of 2.58° [see Fig. 3(b)]. For a separation of 60 mm between both diffusers, the diameter of the spot on the second diffuser amounts to 5 mm.
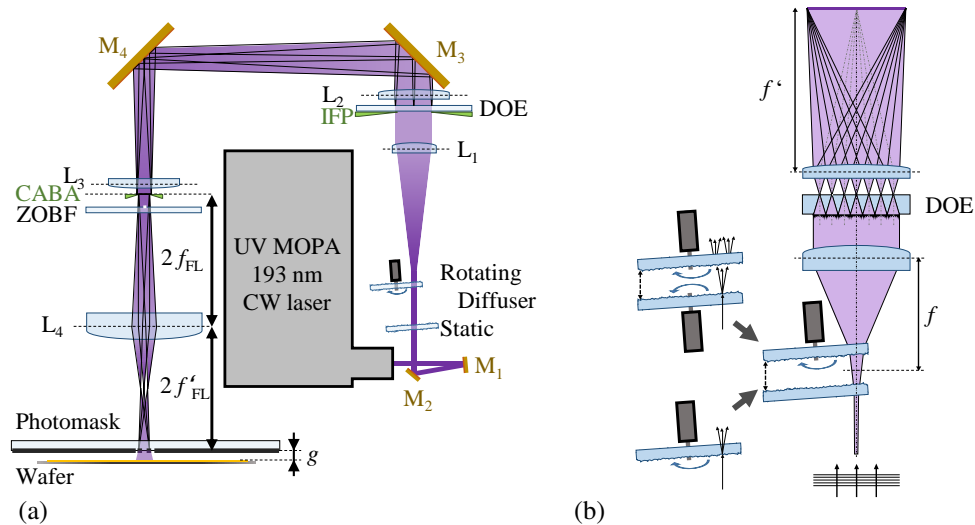

Fig. 2. (a) Optical setup with beam-shaping elements. Depicted are static and rotating diffusers, dielectric mirrors M_{1-4}, condenser lens L_1, illumination filter plate (IFP), diffractive optical element (DOE) in Fresnel configuration, Fourier lens L_2, front lens L_3, changeable area blocking aperture (CABA), zero-order blocking filter (ZOBF), and imaging lens L_4. (b) Diffuser setup to adjust the coherence of the illumination. Different possible combinations of static and rotating diffusers are depicted.

To avoid intensity variations in the mask plane arising from speckle formation, we exploit the integrating nature of the photoresist. Imagine a specific instant in time, with two mutually static diffusers. The speckle pattern formed at this moment in mask and photoresist planes depends on the microscopic configuration of the two diffusers at this point. The rotation of one diffuser with respect to the other varies the speckle pattern, with total statistical independence once the diffuser is moved farther than the lateral speckle size. A temporal integration in the photoresist yields the ensemble average, practically eliminating speckle [20, 24]. This temporal averaging over independent speckle fields also mitigates the possible effects of temporal coherence of the
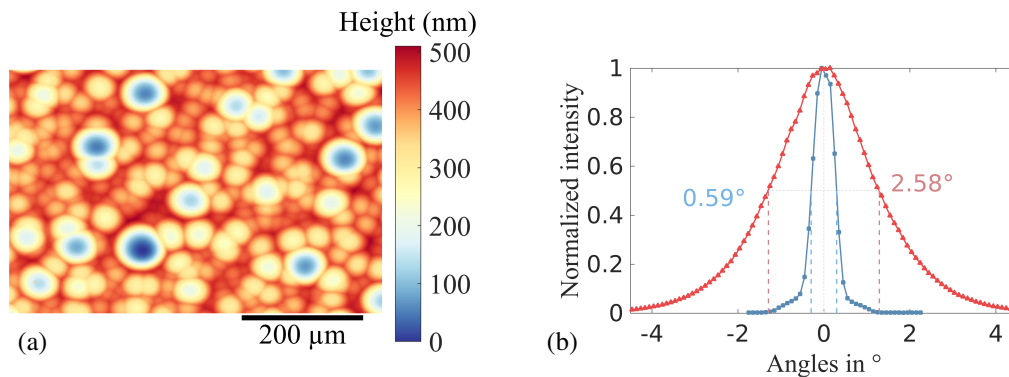
Fig. 3. (a) White light interferometric image of a shaped random diffuser. (b) Goniometric measurements of static (blue dots) and rotating (red triangles) diffusers. The full width at half maximum (FWHM) is denoted.

illuminating light source.

In addition, subsequent homogenizers also help in controlling the speckle size. Each beamlet generated by the mixing element of a homogenizer can be interpreted as a secondary source. The superposition of all these beamlets in the homogenizers' Fourier plane leads to a decrease in lateral coherence [25]. Our homogenization setup is discussed in section 2.4.

The ability of speckle to interfere, expressed as the coherence length, is given by the correlation between the intensity distribution at two points of a speckle pattern. This coherence length coincides with the average size of a speckle [26]. According to [27, 28], the $1/e$ speckle size in radial and longitudinal directions are calculated as the normalized correlation function of a developing speckle pattern (Eqn. (4) of [28]). As this relation is derived for a paraxial system with thin-lens approximation it serves to illustrate the order of magnitude. Furthermore, the results are valid only for fully developed speckle, i.e. speckle in the Fraunhofer far-field regime. Since lens L_1 in our setup performs a Fourier transform on the propagating beam, we can consider any position behind the lens to be in the far field, thus showing fully developed speckle. The radial speckle diameter on the DOE amounts to approximately $10\,\mu m$. In comparison, the subaperture diameters on the DOE are $\approx 2\,mm$, and, consequently, incoherent illumination can be assumed.

To suppress interference effects caused by the Fabry-Perot response of optical elements in the setup, the longitudinal coherence length has to be considered. The $1/e$ length of speckle incident on the mixing element of the diffuser can be calculated as $\approx 1\,mm$, following the same approach introduced in [28]. This is shorter than the optical path length (OPL) for multiple reflections of any element in our illumination setup (here OPL $= 2 \cdot d \cdot n$ of an element of thickness d and refractive index n). Solely the proximity gap between photomask and substrate of $\leq 20\,\mu m$ as well as the photoresist are considerably thinner. To avoid interference fringes, parallel leveling of photomask and substrate is crucial as any error in parallelism causes fringes. In our setup, we use reflectometric sensors in conjunction with a high-precision six-axis positioning stage to achieve precise leveling.

Further optimization requires applying a bottom anti-reflective coating (BARC) between wafer and photoresist, typically implemented to avoid the formation of standing waves within the photoresist [14].

2.4. Illumination homogenizing

To realize uniform illumination in the mask plane, we implement the principle of a non-imaging homogenizer [29]: A micro-optical mixing element divides an incoming light field into individual beamlets, which in turn are superimposed by a spherical lens in its focal plane. The lens is

typically referred to as Fourier lens (focal length of 200 mm). We use an eight-level DOE in Fresnel design featuring a hexagonal array of Fresnel lenslets with half-axis of 1.9 mm and 2.2 mm, optimized for a wavelength of 193 nm. It is illuminated by the speckle field arising from the diffuser setup, as shown in Figure 2.

The eight-level DOE possesses a theoretical maximum diffraction efficiency of 95 % [30], which is not reached with the element in use. This non-unity efficiency leads to a strong zeroth order in the Fourier plane, restraining the uniformity. To mitigate this effect, we introduce an opaque circular aperture, designated zero-order blocking filter (ZOBF). By placing this element not directly in the superposition plane, but slightly out of focus, it is possible to soften the intensity spike instead of blocking it. This results in an overall uniform intensity, as demonstrated in section 3.

The principle of two staged diffusers is solved in an integrated way. We chose shaped random diffusers for our diffuser setup. These diffusers consist of a multitude of convex facets, all with close similarity in shape but with random arrangement across the surface, as depicted in Fig. 3(a). In the far field, their behavior is equivalent to standard ground glass diffusers in terms of causing speckle while offering known divergence angles. This enables the combination of beam shaping and coherence control in one element. In our case, the second diffuser together with the collimation lens acts already as a non-imaging diffuser. An object-side telecentric setup is realized by placing the diffuser in the object-side focal plane of the lens (or rather by placing the diffuser such that the focal point of an on-axis facet and the focal point of the collector lens coincide). Due to restriction in space, we had to place the DOE close to the collimator lens, closer than the collimator lens' focal length. Thus, the superposition of the beamlets emerging from the diffusers is not complete. The DOE is not uniformly illuminated, which can be seen in the measured angular spectra shown in Fig. 4 later on. We deem this less important than underfilling the hole free diameter of the DOE.

3. Ray-tracing simulation and measurement of mask-aligner illumination

3.1. Coherent and incoherent simulation of illumination

Simulating coherent light sources typically requires a rigorous solution of Maxwell's equations to incorporate the full nature of coherence. This is typically not included in large-scale optical modeling as ray-tracing [31], and the modeling of diffusers thus requires an exact model of their surface. Moreover, calculating array optics is likewise not trivial [32, 33]. Despite using a coherent light source, a fully coherent simulation is not necessary, exploiting the following properties of our setup: long exposure times with respect to diffuser rotation speed, the time-continuous output of our laser, and the integrating nature of the photoresist.

After passing the rotating diffuser, the laser beam forms a speckle field, which is uncorrelated with respect to every continuous position of the rotating diffuser for displacement due to rotations larger than the speckle size as discussed in section 2.3. At the photoresist, the intensity distribution of each diffuser orientation is summed up. This temporal superposition of many interference patterns leads to an overall homogenizing effect. The continuous laser emission facilitates this homogenization. The contrast of the overall speckle pattern scales with $m^{-\frac{1}{2}}$, with m being the number of uncorrelated speckle patterns within the exposure time [20]. For a CW source, the rotation speed of the diffuser is thus not an important parameter, as long as the integration time comprises at least one full diffuser revolution.

This implies for the simulation of the mask-aligner illumination that the overall intensity distribution can be modeled using incoherent sources only. Simulating a diffuser is thus reduced to using sources with random emission angles. Source modeling is further simplified by the design of the shaped random diffusers [20], which leads to a well-known angular distribution of the scattered light. The ray tracing program ZEMAX has been used in all simulations.

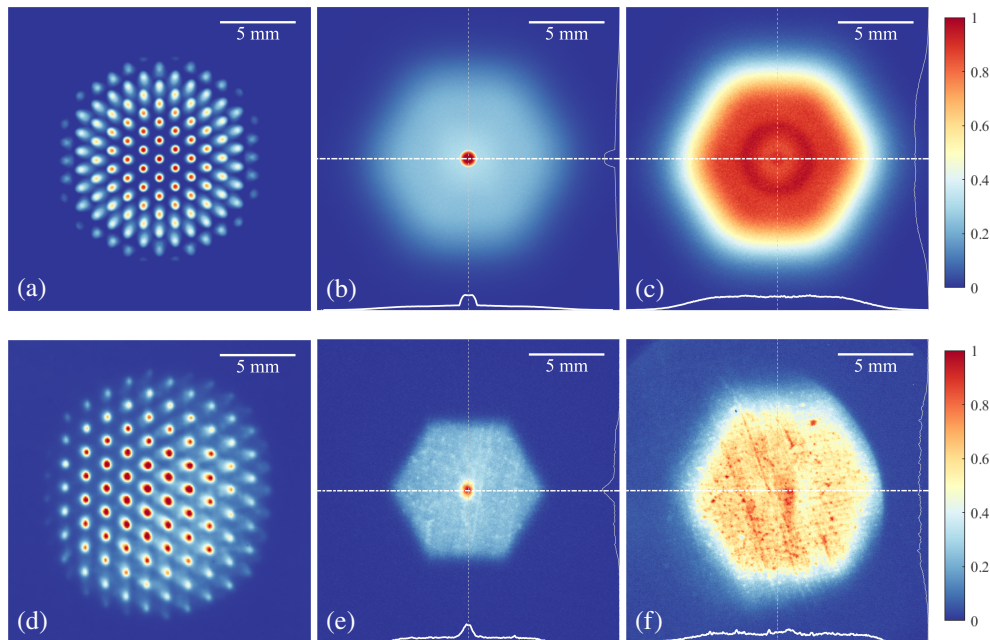## 3.2. Beam shaping with diffuser and DOE

Fig. 4. Upper row: Simulation of the illumination system; intensity distribution in different planes. (a) Single beamlets in a plane conjugated to the DOE. (b) Mask plane intensity distribution without ZOBF. (c) Mask plane intensity distribution with ZOBF. Lower row: measurements of the actual illumination system at the same planes and in similar configuration as (a-c). (d) and (f) were imaged through a 150 mm lens instead of the 200 mm lens used for (e) and are thus scaled by a factor of 1.3.

The illumination setup as implemented in the lab, compare Fig. 2(a), was simulated following the approach described above. The diffuser was modeled by a circular surface source with a diameter of 4 mm and a divergence angle of $3°$. All lenses were simulated using their equivalent lens model in the ZEMAX lens catalog. The lenses $L_{1,2,3}$ each have a focal length of 200 mm (≈ 180 mm at 193 nm). Behind L_1, the beam diameter is roughly 25 mm. The lenslets of the hexagonal Fresnel DOE have a pitch of 1.9 mm and an individual focal length of 15.2 mm. L_4 has a focal length of 150 mm (≈ 135 mm at 193 nm). Simulation results of the intensity in selected planes are shown in Figs. 4(a) to 4(c).

Figures 4(d) to 4(f) show the measured intensities in the same planes and of the same configurations as considered in the simulations. To visualize the 193 nm radiation, a screen was fabricated by applying a fluorescent dye (LUGB 5 from LUMINOCHEM) onto a polymer film, and the beam profile on the screen is captured by a CCD camera. Clumping of the dye particles limited its uniform distribution, thus introducing the dots and granular intensity centers, visible in Figs. 4(e) and 4(f). An improvement of our measurement equipment here is needed and foreseen for future work.

We attribute the scaling mismatch in all three pictures 4(d) to 4(f) to imperfect positioning of the elements in the lab setup. In addition, the performance of the real microlens array is superior to the simulated one, as is visible in Fig. 4(e). A small tilt in the optical axes of the DOE's illumination and the subsequent Fourier lens causes the visible difference between simulation and measurement in Figs. 4(a) and (d), respectively. This difference has no measurable influence

in the printing performance of the system.

By adapting the angular spectrum of illumination to the specific mask design, diffraction effects can be minimized [2, 21], which leads to enhanced resolution and print quality. Angular shaping is a prerequisite for advanced resolution-enhancement techniques, as off-axis illumination and source-mask optimization [34, 35], and demonstrated for amplitude and phase mask in section 4.1 and 4.2, respectively.

Figures 4(a) and 4(d) show the simulation and the measurement of the intensity distribution in different beamlets, respectively. As clearly visible in both figures, the intensity per channel is maximal in the center on the overall optical axis and decreases towards the edges. This intensity distribution originates from the non-uniform illumination of the DOE due to non-ideal spacing of optical elements as discussed in section 2.4.

We define the optical efficiency of our system as the ratio of optical power in the mask plane to the laser output power. For the described setup, the optical efficiency amounts to $\approx 12.5\%$. We would like to point out that the presented setup relies on optical elements without antireflection coatings. At each interface, reflection amounts to about 6% at the considered wavelength. In total, reflection at all interfaces combined with the non-unity efficiency of the DOE (>80%) leads to losses of $\approx 66\%$ in optical power. The beam-shaping itself thus contributes to optical losses by a share of 21.5%, including the intensity attenuation at the ZOBF.

4. Experimental results

As a proof-of-principle, we present lithographic results using 193 nm CW illumination for an amplitude mask and for a chromeless two-level phase mask, both fabricated from UV-grade fused silica. We like to emphasize that although our proof-of-principle results are obtained for a small printing field of $1\,cm^2$, the homogenization principles can be applied to achieve full-field mask-aligner lithography.

Our mask-aligner possesses an ETEL SARIGAN high-precision movement stage to position the photoresist-covered wafer relative to the photomask. The mutual distance is measured with an AVANTES spectroscopic reflectometry setup at three positions, enabling leveling of mask and wafer with sub-micron precision. The DUV photoresist TOK TARF-P6239 ME, optimized for
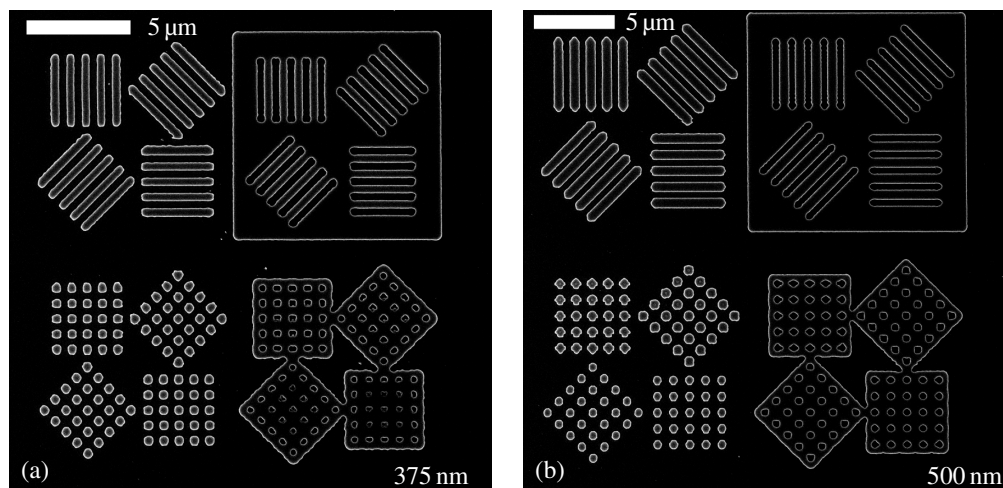

Fig. 5. SEM micrograph of resolution structures in photoresist, patterned in soft contact between mask and wafer. The lines and spaces have critical dimensions of (a) 375 nm and (b) 500 nm.

designs featuring lines and spaces, is spin-coated onto silicon wafers and pre-baked at 110 °C for one minute, resulting in a thickness of 120 nm.

Subsequently, the resist is exposed, with exposure doses adapted to the intensity in the mask plane. Typically, the exposure dose for both amplitude and phase mask amounts to 11 mJ cm^{-2} (measured with a Thorlabs Photodiode S120VC) at a stabilized laser output of 5 mW. Following the exposure, a post-exposure bake (110 °C, 1 min) is conducted on a hotplate, and the resist is developed for one minute in AZ MIF 327 in a puddle process.

4.1. Amplitude mask

The amplitude photomask was fabricated by e-beam lithography and consists of typical lithography resolution structures, featuring lines and spaces, square and circular vias, and their inverse structures. The critical dimension in the mask are directly transferred to the wafer.

Photomask and wafer are brought into soft contact. Print results are depicted in Fig. 5 for critical dimensions of 375 nm and 500 nm. The resolution structures are clearly resolved, and the shapes of squares and spheres are reproduced. Lines and spaces are resolved down to a critical dimension of 375 nm. Squares and holes require a lower exposure dose and have to be optimized separately. The angular spectrum for the illumination possesses a maximum angle of 2.7°.

As discussed before, bringing the mask and the photoresist in contact is not desirable, since it introduces defects and hence reduces the yield and reproducibility of the lithographic process. Mask-aligner lithography in proximity mode is the preferred fabrication technique. Figure 6 shows optical micrographs of lines and spaces with critical dimensions of 1750 nm and 2000 nm, obtained for a proximity gap of 20 μm. Small line-end deviations arise, originating from diffraction, which can be alleviated for example by applying the principle of optical proximity correction (OPC, not included here). The width of the bars depends sensitively on the contrast of the imaging process and the contrast of the resist, and can be adapted by the exposure dose. As described in section 3, the uniformity of the illumination leads to consistent results all over the print field. Similar results are obtained for a proximity gap of 15 μm, as depicted in Fig. 7. In comparison, in mask-aligner lithography using i-line illumination the resolution is typically limited to some 3 μm [36].

In addition, we show etched structures, using a chromium layer as etch stop patterned by lift-off. Figure 8 depicts scanning electron microscope (SEM) images of resolution structures before chromium removal, etched in an ICP-RIE with chlorine chemistry. These results demonstrate that our 193 nm CW laser source can be conveniently used together with prevalent semiconductor technology.
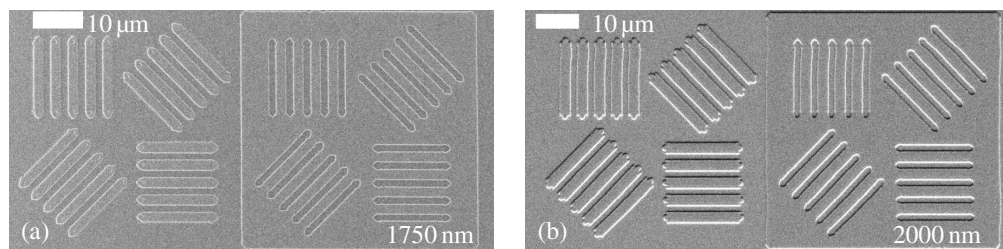

Fig. 6. SEM images of resolution structures in photoresist, patterned with a proximity gap of 20 μm. Here the lines and spaces have critical dimensions of (a) 1750 nm and (b) 2000 nm. The emergence of line-end deviations are caused by diffraction, and can be improved by principles of optical proximity correction (OPC).
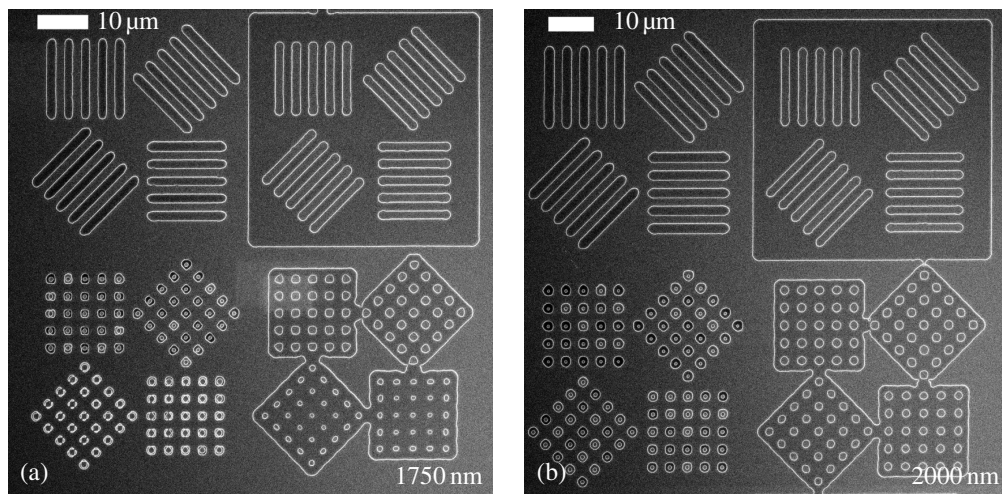
Fig. 7. SEM images of resolution structures in photoresist, patterned with a proximity gap of 15 μm between mask and wafer. The lines and spaces have critical dimensions of (a) 1750 nm and (b) 2000 nm.

4.2. Phase mask

In order to tap the full potential of our setup, we apply a two-level phase mask, with a step height corresponding to a phase shift of π. Essentially, gratings with different periods and hexagonal hole arrays have been fabricated (see Fig. 9). The illumination is adapted to obtain near-plane-wave illumination by selecting only small illumination angles. This is achieved by inserting a circular illumination filter plate (IFP) in front of the DOE, i.e. only the central channels contribute to the illumination (compare section 3.2). The seven spots in the center are transmitted, see Fig. 4(a), corresponding to illumination angles centered around 0° and 0.57°.

We show here line gratings with a half-pitch of 500 nm in proximity lithography featuring a gap of 20 μm, see Fig. 9(a). Larger periods have also been realized. The visible edge roughness might originate from minor variations in the dose reaching the photoresist and can be addressed by further exposure dose optimizations.

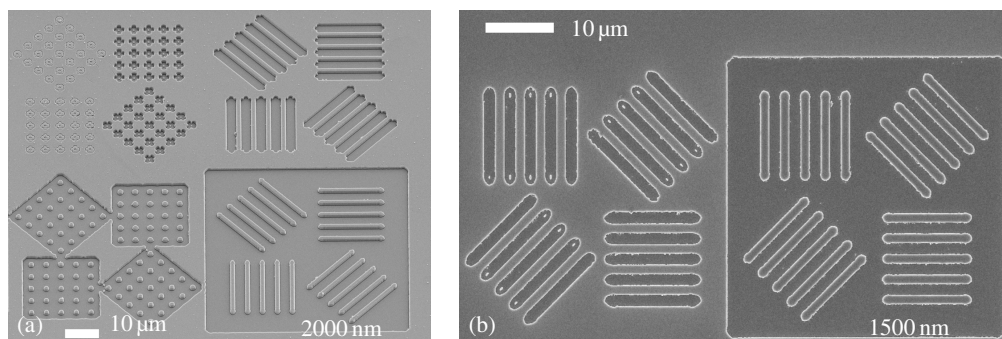Furthermore, we demonstrate a hole array in hexagonal arrangement with a center-to-center

Fig. 8. SEM micrographs of etched structures in silicon, still covered with chromium etch mask, which has been patterned with a proximity gap of 10 μm between photomask and wafer. The lines and spaces have critical dimensions of (a) 2000 nm and (b) 1500 nm, and the etch depth is approximately 800 nm and 400 nm, respectively.

distance of 650 nm, as depicted in Fig. 9(b). Such patterns are required for example to fabricate photon multipliers [37] or photonic crystals for bio-sensing [38]. Mask-aligner lithography represents a cost-effective fabrication technology for hole arrays compared to wafer steppers (expensive), e-beam lithography (slow), or nano-imprint (yield).

We would like to point out two aspects for future development: Due to the high coherence of the source, in principle it is possible to directly illuminate the phase mask, by simply introducing a beam expansion to cover the desired field size. However, due to the inhomogeneous beam profile of the laser beam, see Fig. 1(b), additional beam homogenization is required. Moreover, beam shaping can also be integrated into the laser housing to achieve a Gaussian or flat-top output by default.
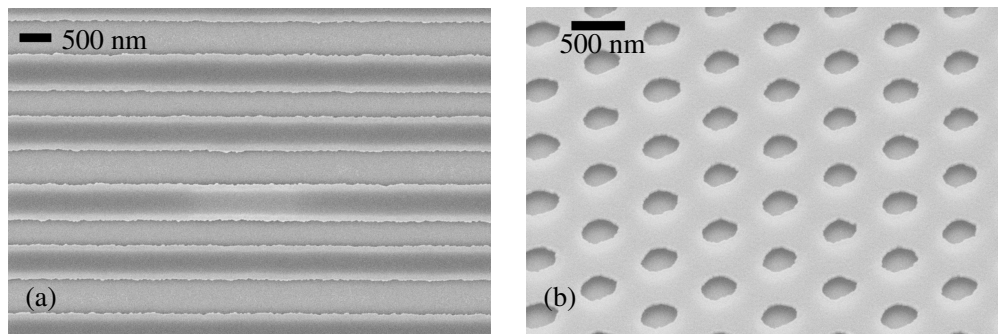

Fig. 9. Periodic structures in photoresist using a phase mask, patterned with a proximity gap of 20 μm between mask and wafer. The grating period in (a) amounts to 1 μm, and the center-to-center distance in (b) is 650 nm.

5. Conclusion

We present in a proof-of-principle experiment the suitability of a 193 nm CW diode laser as a light source for high-resolution mask-aligner lithography. The optical performance is comparable to prevalent excimer light sources in the DUV, while the continuous-wave operation of our light source features an improvement in ease of implementation, source stability, and thermal heat load. Our investigation comprises both soft-contact and proximity exposures. Standard amplitude photomasks (chromium layer on fused silica substrate) as well as chromeless two-level phase masks have been investigated.

We designed at first the necessary illumination system incorporating the DUV laser light source and presented it. A beam shaping concept for mask-aligner illumination at 193 nm has been introduced, characterized, and discussed. Diffractive optical elements (DOE) with hexagonally arranged eight-level Fresnel lenslets have been integrated. In the flat-top intensity distribution shaped with the DOE, a strong intensity spike caused by a zero-order contribution has been both simulated and observed, whereas the effect is less pronounced in observation than expected from simulation. It has been shown how the introduction of a defocused blocking aperture allows for correction of this intensity spike, thus enabling uniform illumination in the mask plane. The introduction of a set of rotating and fixed shaped diffusers proved sufficient to avoid interference effects in the photoresist, emerging from the highly coherent laser beam. Upon integrating the source into the actual photolithographic system, we have also assessed its actual performance. The print resolution improvement in mask-aligner lithography anticipated by introducing a DUV light source follows the expectations: Lines and spaces structures with minimum feature sizes of < 2 μm were printed with a proximity gap of up to 20 μm. In addition, in soft contact we demonstrate resist structures (lines and spaces) with minimum feature size of 375 nm with a binary mask.

Further improvement can be achieved by implementing an illumination setup with refractive microoptical Koehler integrators. This is expected to increase the illumination uniformity and hence the overall performance. Furthermore, it is worthwhile to study the difference between imaging and non-imaging Koehler integrators for laser beam shaping. Based on the high coherence and thus good collimation of the laser, no major differences between the two setups are expected.

The intensity homogenization of the illumination setup for phase mask exposures requires also further optimization. Here, the difficulties arise from the need of plane wave illumination incident normal to the mask surface, while at the same time controlling the coherence length to not suffer from Fabry-Perot interferences of optical elements in the beam path.

Industrial applications require the full exposure of large substrates. This can be realized either by scaling the optics to full-field exposure or by stitching exposure fields of intermediate size. The former requires a simple upscaling of optical elements. The latter allows to use small high-resolution photomasks, which can be fabricated at reasonable prices, for full substrate exposure by stepping.

Finally, to maintain reasonably short exposure times, an increase of the laser output power is necessary. This can eventually be realized by improving the SHG in the KBBF crystal. With such an upgrade, optical lithography relying on continuous-wave DUV lasers might be within reach.